



Topologically controlled phase transitions and nanoscale film self-assemblies of cage poly(ϵ -caprolactone) and its counterparts

Journal:	<i>Polymer Chemistry</i>
Manuscript ID	PY-ART-11-2020-001567.R2
Article Type:	Paper
Date Submitted by the Author:	07-Jan-2021
Complete List of Authors:	Ree, Brian; Hokkaido University, Faculty of Engineering Mato, Yoshinobu; Hokkaido University, Graduate School of Chemical Science and Engineering Li, Xiang; Pohang University of Science and Technology, Chemistry Kim, Jehan; Pohang University of Science & Technology, Pohang Accelerator Laboratory Isono, Takuya; Hokkaido University, Faculty of Engineering Satoh, Toshifumi; Hokkaido University, Division of Applied Chemistry, Faculty of Engineering

Topologically controlled phase transitions and nanoscale film self-assemblies of cage poly(ϵ -caprolactone) and its counterparts†

Brian J. Ree,^{a,+} Yoshinobu Mato,^{b,+} Li Xiang,^c Jehan Kim,^d Takuya Isono,^a and Toshifumi Satoh^{a,*}

^aFaculty of Engineering, Hokkaido University, Sapporo 060-8628, Japan

^bGraduate School of Chemical Sciences and Engineering, Hokkaido University, Sapporo 060-8628, Japan

^cDepartment of Chemistry, Pohang University of Science and Technology, Pohang 37673, Republic of Korea

^dPLS-II Beamline Division, Pohang Accelerator Laboratory, Pohang 37673, Republic of Korea

⁺B. J. Ree and Y. Mator equally contributed to this work.

[†]Electronic supplementary information (ESI) available: Grazing incidence X-ray scattering (GIXS) data analysis, Fig. S1, Fig. S2, synthesis, Schemes S1-S4, and Fig. S3-S10. See DOI: 10.1039/

ABSTRACT: Here we report the first quantitative investigation of nanoscale film morphologies of a cage-shaped poly(ϵ -caprolactone) (*cg*-PCL_{9k}) and its counterparts in star, cyclic, and linear topologies (*st*-PCL_{9k}, *cy*-PCL_{6k}, and *l*-PCL_{6k}) with consideration of topological influence through synchrotron grazing incidence X-ray scattering analysis. The folded crystalline layer thickness l_c is found to be in the increasing order of: *st*-PCL_{9k} < *l*-PCL_{6k} < *cy*-PCL_{6k} < *cg*-PCL_{9k}. Additional structural parameters, such as lamellar orientation, crystallinity, and orientation of orthorhombic lattice in nanoscale film, exhibit intricate dependencies on their molecular topologies and steric influences from the molecular joints and end groups. Nevertheless, all topological PCLs form lamellar structures based on orthorhombic crystal lattice in nanoscale films. In addition, crystallization temperature T_c and crystal melting temperature T_m of all PCLs in bulk are highly dependent on the molecular topology; both T_c and T_m follow the same increasing trend of: *st*-PCL_{9k} < *l*-PCL_{6k} < *cy*-PCL_{6k} < *cg*-PCL_{9k}. Phase transition characteristics such as heat of fusion and crystallinity in bulk state, and thermal stability also depend upon the topological and steric influences.

Keywords: cage poly(ϵ -caprolactone), star poly(ϵ -caprolactone), two-point jointed cyclic poly(ϵ -caprolactone), linear block poly(ϵ -caprolactone), topology effects, phase transitions, nanoscale film morphologies, lamellar structure, orthorhombic lattice, structural parameters, crystallinity

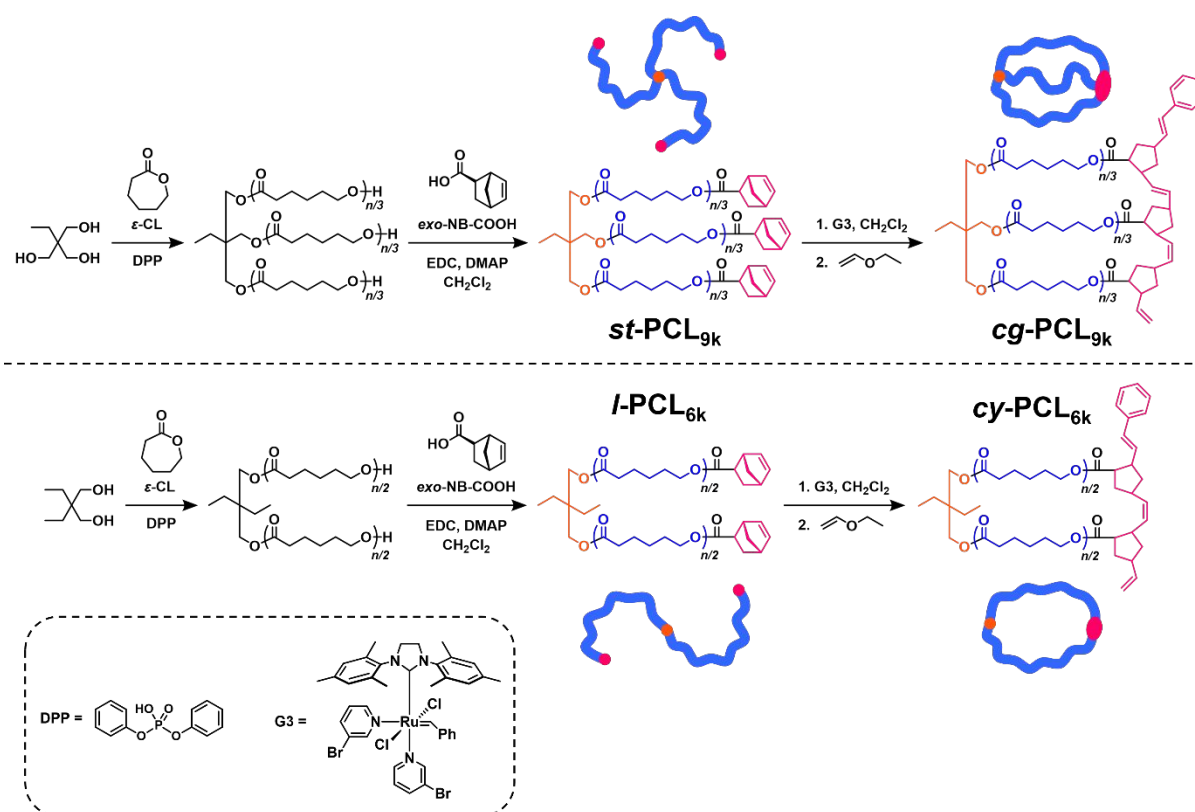
Introduction

Nanoscale cages are a unique and attractive form of materials to academia and industry because of their potential to be used in various applications such as capsules, carriers, templates, reactors, and so on.¹⁻⁵ In general, they can be prepared through two methods: (i) self-assembly of molecules^{1,2,6-14} and (ii) chemical synthesis of molecular cages.^{3-5,15-17} The self-assembly approach has been practiced in various ways so far, and a number of physically assembled cages in various sizes, topologies, and functionalities have been reported as a result.^{1,2,6-14} However, physically assembled cages are known to be sensitive to various factors regarding the surrounding environment such as pH, temperature, solvent type, and other chemical ingredients, which could easily alter their structural dimensions and stability. As alternatives for overcoming the limitations of physically assembled cages, great research effort began developing synthetic molecular cages in the form of organic molecule-based cages.^{3-5,15-18} Over the years, several macromolecular cages have been reported, which are based on polytetrahydrofuran,¹⁹⁻²³ polystyrene,²⁴⁻²⁷ poly(ϵ -caprolactone) (PCL),^{28,29} poly(ethylene oxide)³⁰, and poly(*n*-decyl glycidyl ether-*block*-2-(2-(2-methoxyethoxy)ethoxy)ethyl glycidyl ether).³¹ Despite the success in synthesizing unique cage materials, however, the inherent difficulties in the well-defined synthesis and effective purification leave the comprehension of their fundamental aspects such as morphology and physical properties in an early, developing stage.

From the perspective of molecular topology, molecular cages are expected to present many fascinating aspects yet to be discovered as their cage topology is comparable to cyclic topology with respect to the absence of chain ends. The inherent topological resemblance to cyclic polymers suggest molecular cages to exhibit similar trends in physical properties and morphology, in which several reports demonstrate the cyclic PCLs presenting higher melting and crystallization

temperature,³²⁻³⁴ higher crystallinity,³² higher degradation temperature,³² and higher melt density,³⁴ and faster crystallization kinetics³³ at a chosen temperature, but slower crystallization kinetics³³ at a given degree of supercooling than the linear PCL counterparts, as well as key aspects of lamellar morphology in thin film being impacted by the absence of chain ends.³⁴ Additionally, because the precursors of molecular cages exhibit star topology, the discussion regarding the effect of drastic topological transformation is necessary. There are a few reports that explore the differences in the thermal properties and morphological aspects of cage-shaped PCLs and their star-shaped precursors,^{28,29} but the depth of characterization and analysis does not provide sufficient discussions.

To address the extent of topological influences of cage topology in a more rigorous manner, this study reports on the nanoscale film morphological details and chain conformations of cage-shaped, semi-crystalline PCL (*cg*-PCL_{9k}) and its star-shaped (*st*-PCL_{9k}), cyclic (*cy*-PCL_{6k}), and linear (*l*-PCL_{6k}) counterparts using quantitative synchrotron grazing incidence small and wide angle X-ray scattering (GISAXS and GIWAXS) analysis. Additionally, the thermal characteristics and phase transitions of the topological PCLs have been investigated by thermogravimetry (TGA) and differential scanning calorimetry (DSC). The four topological PCLs in this study have been synthesized according to the synthetic schemes (Scheme 1) reported in our previous paper,²⁸ where ring-opening metathesis oligomerization of norbornene end groups was used to form the cage and cyclic PCLs from their respective star and linear precursors; the synthetic details are described in Electronic Supplementary Information (ESI†) and the molecular characteristics are listed in Table 1. To effectively discuss the impact of topological influence, the molecular weight of each PCL segments from the initiator has been fixed at 3,000 g mol⁻¹ with dispersity *D* values less than 1.08 for all polymers.



Scheme 1 Topological poly(ϵ -caprolactone)s and their synthetic schemes: *cg*-PCL_{9k}, a cage-shaped PCL containing two molecular joints, is obtained by the cage-formation of its precursor *st*-PCL_{9k}, a star-shaped PCL containing one molecular joint, where the three hydroxyl end groups are capped with *exo*-NB-COOH; *cy*-PCL_{6k}, a cyclic PCL containing two molecular joints, which is obtained by the cyclization of its precursor *l*-PCL_{6k}, a linear PCL based on one molecular joint, where the two hydroxyl end groups are capped with *exo*-NB-COOH. G3: Grubbs' catalyst 3rd generation; CH₂Cl₂: methylene chloride; ϵ -CL: ϵ -caprolactone; DPP: diphenyl phosphate; *exo*-NB-COOH: (\pm)-*exo*-5-norbornenecarboxylic acid; EDC: 1-ethyl-3-(3-(dimethylamino)propyl)-carbodiimide hydrochloride; DMAP: *N,N*-dimethyl-4-aminopyridine.

Table 1. Fundamental characteristics of the synthesized *cg*-PCL_{9k} and its counterparts in various topologies (*st*-PCL_{9k}, *cy*-PCL_{6k}, and *l*-PCL_{6k})

Topological PCL	$M_{n,\text{NMR}}^a$ (g mol ⁻¹)	$M_{n,\text{SEC}}^b$ (g mol ⁻¹)	\bar{D}^c	$T_{d,5}^d$ (°C)
<i>cg</i> -PCL _{9k}	10,600	11,900	1.08	375
<i>st</i> -PCL _{9k}	10,600	14,700	1.05	377
<i>cy</i> -PCL _{6k}	6,500	8,500	1.08	376
<i>l</i> -PCL _{6k}	6,500	9,800	1.04	370

^aNumber-average molecular weight determined in deuterated chloroform (CDCl₃) by proton nuclear magnetic resonance (¹H NMR) spectroscopy analysis. ^bNumber-average molecular weight determined by size exclusion chromatography (SEC) in tetrahydrofuran (THF) using polystyrene standards. ^cDispersity determined by SEC in THF using polystyrene standards. ^dTemperature at which 5.0 wt % weight loss occurred in TGA run with a ramping rate of 10 °C min⁻¹ under nitrogen atmosphere.

Experimental

For the bulk PCL samples, TGA and DSC analyses were carried out under nitrogen atmosphere using Hitachi instruments (model STA7200 and model DSC7020, Hitachi Instrument, Tokyo, Japan).

For the individual topological polymers, solutions with a concentration of 0.5 wt% were prepared in tetrahydrofuran and filtrated with polytetrafluoroethylene filter membranes (0.2 μm pore size). Each solution was spin-cast onto silicon substrates and then followed by drying in vacuum at room temperature for 24 h, giving 96–120 nm thick films. The film thicknesses were measured by using a spectroscopic ellipsometer (Model M-2000, Woollam, Lincoln, NE, USA). The films were kept in a drying chamber at room temperature before use.

For the nanoscale PCL films, all GISAXS and GIWAXS measurements were carried out with a two-dimensional (2D) charge-coupled detector (CCD) (model Rayonix 2D SX 165, Rayonix, Evanston, IL, USA) at the 3D Beamline of the PLS-II facility (3.0 GeV power, 400 mA), Pohang Accelerator Laboratory, Pohang, Korea.³⁵ The incident X-ray beam had a wavelength λ of 0.12296 nm, and the incidence angle α_i was set in the range of 0.1240–0.1400° with respect to the film plane. GISAXS measurements were conducted at a sample-to-detector distance (SDD) of 2926.0 or 2947.1 mm, whereas GIWAXS measurements were performed at SDD = 209.0 or 210.9 mm. The scattering data collection time ranged from 10 to 30 s. All scattering measurements were conducted at room temperature. The scattering angles were corrected by using a precalibrated polystyrene-*block*-poly(ethylene-*random*-butylene)-*block*-polystyrene and silver behenate standards (Tokyo Chemical Ind., Tokyo, Japan); the positions of the X-ray beams reflected from the silicon substrate were used additionally.

Results and Discussion

Thermal Stability and Phase Transitions. All topological PCLs in bulk states reveal a single-step degradation behaviors regardless of the topologies, as shown in Figs. 1a-1, 1b-1, 1c-1 and 1d-1. However, the degradation temperature is found to vary slightly with the topologies. The temperature at which the first 5% mass loss occurs ($T_{d,5}$) is 375 °C for *cg*-PCL_{9k}, 377 °C for *st*-PCL_{9k}, 376 °C for *cy*-PCL_{6k}, and 370 °C for *l*-PCL_{6k} (Table 1). *cg*-PCL_{9k} and *cy*-PCL_{6k} exhibit $T_{d,5}$ that is 5 to 6 °C higher than that of the linear counterpart, which indicates that the absence of chain ends in their topologies slightly enhances their thermal stability. Surprisingly, *st*-PCL_{9k} reveals highest $T_{d,5}$ of 377 °C despite having three chain ends. This denotes that norbornene end groups enhance the thermal stability of the *st*-PCL_{9k}. The 7 °C difference in the $T_{d,5}$ values for *l*-PCL_{6k} and *st*-PCL_{9k} may be attributed to the fact that *st*-PCL_{9k} has a relatively higher molecular weight than *l*-PCL_{6k} that introduces a notable increase in thermal stability for the star polymer.

The topological PCLs in bulk states have been further characterized with DSC analysis regarding their phase transition behaviors. In the first cooling with a ramping rate of 10.0 °C min⁻¹ from the melt state (70 °C), *cg*-PCL_{9k} exhibits a single exothermic peak originating from the crystallization of the ϵ -CL repeating units, as shown in Fig. 1a-2; here, the exothermic peak maximum appears at 26.9 °C (= $T_{c,max}$, crystallization temperature). The exothermic peak (i.e., nonisothermal crystallization peak) is also observed when measured with slower ramping rates (5.0 and 2.0 °C min⁻¹). Slower ramping rates leads to a crystallization peak of higher $T_{c,max}$, which results from a combination of the nonisothermal crystallization kinetics and relatively poor thermal conductivity of the polymer. Similar trends of single exothermic peaks are observed in the cooling runs of *st*-PCL_{9k}, *cy*-PCL_{6k}, and *l*-PCL_{6k} (Figs. 1b-2, 1c-2, and 1d-2). The representative phase transition parameters determined from the DSC thermograms measured with a ramping rate of 10.0 °C min⁻¹ (cooling and heating) are summarized in Table 2. For consistency, the DSC thermograms measured with 10.0 °C min⁻¹ ramping rate (indicated by black line in Fig. 1) is referred throughout the discussion unless specified.

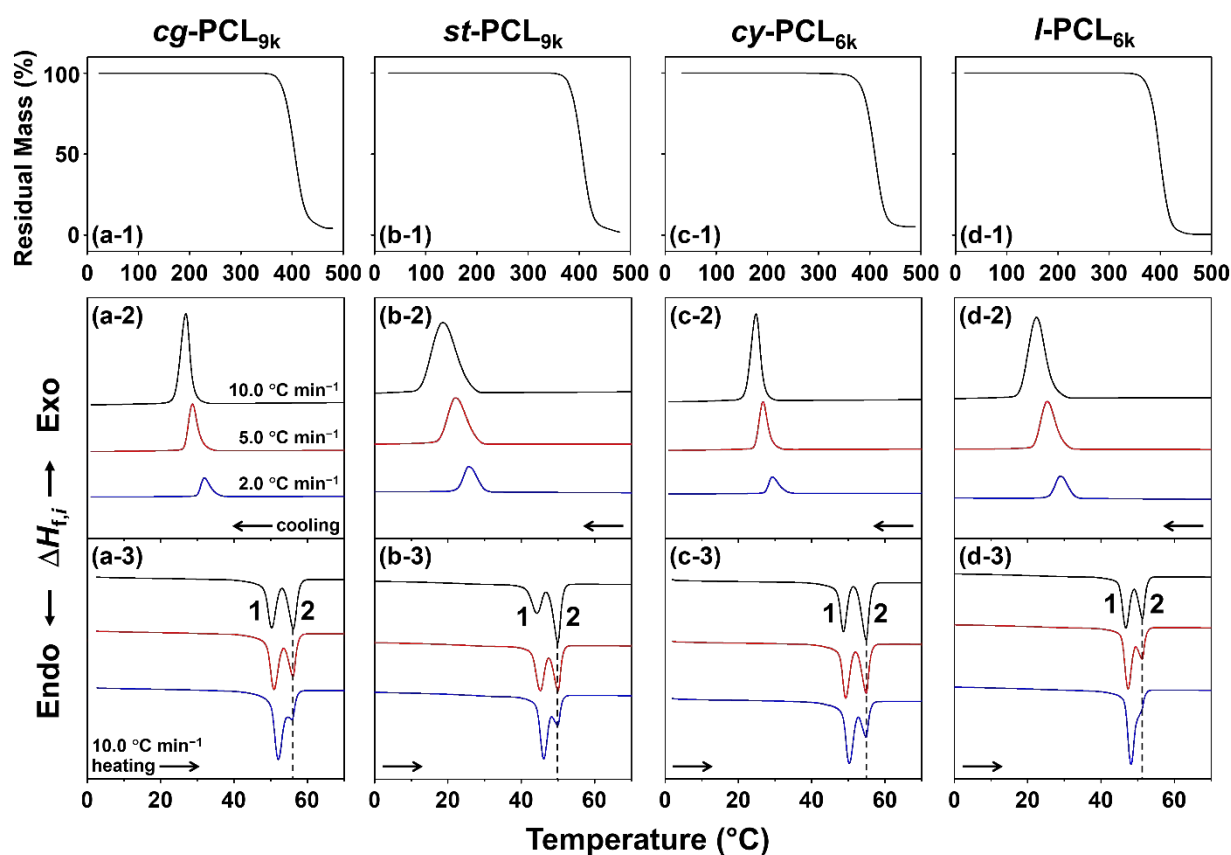


Fig. 1 TGA and DSC thermograms of topological PCLs in bulk measured under nitrogen atmosphere: (a-1, b-1, c-1, d-1) TGA thermograms measured at a rate of 10.0 °C min⁻¹; (a-2, b-2, c-2, d-2) DSC thermograms of the first cooling measured at various rates (black line = 10.0 °C min⁻¹, red line = 5.0 °C min⁻¹, and blue line = 2.0 °C min⁻¹); (a-3, b-3, c-3, d-3) DSC thermograms of subsequent heating following the corresponding first cooling measured at 10.0 °C min⁻¹.

Table 2. Phase transition characteristics of *cg*-PCL_{9k} and its counterparts in various topologies (*st*-PCL_{9k}, *cy*-PCL_{6k}, and *l*-PCL_{6k}) in bulk

Polymer	$T_{c,max}^a$ (°C)	$-\Delta H_{f,c}^b$ (J g ⁻¹)	$-X_{c,c}^c$ (%)	T_{m1}^d (°C)	T_{m2}^e (°C)	$\Delta H_{f,m1}^f$ (J g ⁻¹)	$\Delta H_{f,m2}^g$ (J g ⁻¹)	$\Delta H_{f,m}^h$ (J g ⁻¹)	$X_{c,m1}^i$ (%)	$X_{c,m2}^j$ (%)	$X_{c,m}^k$ (%)
<i>cg</i> -PCL _{9k}	26.9	79.8 ^l (75.3) ^m	57.1 ⁿ (54.0) ^o	50.3	56.1	43.3 ^l (40.9) ^m	36.7 ^l (34.6) ^m	80.0 (75.5)	31.0 ⁿ (29.3) ^o	26.3 ⁿ (24.8) ^o	57.3 (54.1)
<i>st</i> -PCL _{9k}	18.7	64.0 (61.5)	47.8 (45.9)	44.3	49.9	24.7 (24.3)	38.3 (37.9)	62.2 (59.7)	18.2 (17.5)	28.2 (27.1)	46.4 (44.6)
<i>cy</i> -PCL _{6k}	24.8	87.5 (81.4)	62.8 (58.4)	48.7	54.9	43.8 (40.7)	46.2 (43.0)	90.0 (83.7)	31.4 (29.2)	33.1 (30.8)	64.5 (60.0)
<i>l</i> -PCL _{6k}	22.4	68.0 (64.6)	51.3 (48.7)	46.8	51.3	39.6 (37.6)	28.6 (27.2)	68.2 (64.8)	29.9 (28.4)	21.5 (20.5)	51.4 (48.9)

^aCrystallization temperature of PCL segments determined from the peak maximum of the exothermic crystallization transition measured by DSC analysis under nitrogen atmosphere and a temperature ramping rate of 10.0 °C min⁻¹. ^bHeat of fusion generated from the crystallization transition. ^cCrystallinity estimated from the heat of crystallization assuming $\Delta H_c^\circ = 139.5 \text{ J g}^{-1}$ for ideal PCL crystal (ref.#36). ^dCrystal melting temperature of PCL determined from the maximum of the endothermic crystal melting peak **1**. ^eCrystal melting temperature of PCL determined from the maximum of the endothermic crystal melting peak **2**. ^fHeat of fusion estimated from the crystal melting peak **1**. ^gHeat of fusion estimated from the crystal melting peak **2**. ^hTotal heat of fusion estimated from the crystal melting peak of only PCL part. ⁱCrystallinity estimated from the heat of fusion involved in crystal melting peak **1** under assuming $\Delta H_m^\circ = -\Delta H_c^\circ$ for ideal PCL crystal. ^jCrystallinity estimated from the heat of fusion involved in crystal melting peak **2** under assuming ΔH_m° for ideal PCL crystal. ^kOverall crystallinity estimated from the total heat of fusion involved in crystal melting peaks under assuming ΔH_m° for ideal PCL crystal. ^lHeat of fusion of only PCL part estimated from the phase transition. ^mHeat of fusion estimated from the phase transition with respect to the total weight of polymer sample. ⁿCrystallinity of only PCL part estimated from the heat of fusion of the phase transition. ^oCrystallinity estimated from the heat of fusion of the phase transition with respect to the total weight of polymer sample.

The width of nonisothermal crystallization peak at a given cooling rate exhibits the following trend: $cg\text{-PCL}_{9k} < cy\text{-PCL}_{6k} \ll l\text{-PCL}_{6k} \ll st\text{-PCL}_{9k}$. Additionally, the $T_{c,max}$ values show the opposite trend of: $st\text{-PCL}_{9k} \ll l\text{-PCL}_{6k} < cy\text{-PCL}_{6k} < cg\text{-PCL}_{9k}$. These results inform that $cg\text{-PCL}_{9k}$ tends to undergo crystallization in the relatively narrowest and highest range of temperature as well as the shortest duration, whereas $cy\text{-PCL}_{6k}$ will crystallize over a slightly wider temperature range. As for $st\text{-PCL}_{9k}$, its behavior is somewhat similar to $l\text{-PCL}_{6k}$ but its crystallization occurs at a lower temperature and a longer duration.

Collectively, these results inform that $cg\text{-PCL}_{9k}$ and $cy\text{-PCL}_{6k}$ hold advantages over $st\text{-PCL}_{9k}$ and $l\text{-PCL}_{6k}$ regarding crystallization due to their cage and cyclic topologies enabling the PCL segments to retain relatively closer distances. Moreover, the absence of chain ends decreases the degree of freedom with respect to the chain conformation of PCL segments, thereby further enhancing the crystallization of $cg\text{-PCL}_{9k}$ and $cy\text{-PCL}_{6k}$. Between $cg\text{-PCL}_{9k}$ and $cy\text{-PCL}_{6k}$, the cyclic-shape topology proves to be more effective in promoting crystallization. In contrast, the star topology causes penalty in the crystallization of PCL, largely due to the involvement of three chain ends as opposed to none or two of cage, cyclic, and linear topologies.

Both the heat of nonisothermal crystallization ($\Delta H_{f,c}$) and resulting crystallinity ($X_{c,c}$) are in the increasing order: $st\text{-PCL}_{9k} < l\text{-PCL}_{6k} \ll cg\text{-PCL}_{9k} \ll cy\text{-PCL}_{6k}$. These confirm again that the cage and cyclic topologies effectively promote PCL crystallization whereas the star topology

reduces crystallization. Surprisingly, *cg*-PCL_{9k} shows lower $\Delta H_{f,c}$ and $X_{c,c}$ values than those of *cy*-PCL_{6k} despite exhibiting higher $T_{c,max}$ and narrower crystallization peak. These unexpected results may be attributed to different bulkinesses in one of the two molecular joints (the initiator and oligonorbonene moieties). The joint formed by the initiator in *cg*-PCL_{9k} is nearly identical with that of *cy*-PCL_{6k} regarding the chemical structure and sterics, but the second joint formed by three norbonene groups in *cg*-PCL_{9k} is relatively bulkier than that of *cy*-PCL_{6k} (see the chemical structures in Scheme 1). The bulkier joint of *cg*-PCL_{9k} may produce negative contribution to the nonisothermal crystallization, ultimately reducing the magnitude of $\Delta H_{f,c}$ and $X_{c,c}$.

For the subsequent heating with a ramping rate of 10.0 °C min⁻¹ following the first cooling from the melt, *cg*-PCL_{9k} shows two crystal melting peaks rather than a single melting peak: one peak appears at 50.3 °C (= T_{m1} , crystal melting temperature **1**) and another peak appears at 56.1 °C (= T_{m2} , crystal melting temperature **2**) (Fig. 1a-3). Two crystal melting peaks are also discernible in the subsequent heating following the cooling runs with ramping rates of 5.0 and 2.0 °C min⁻¹. Similar two crystal melting behaviors are observed for all other counterparts (Fig. 1b-3, 1c-3, and 1d-3). The analysis results of the endothermic peaks measured at 10.0 °C min⁻¹ are listed in Table 2. These two crystal melting endothermic behaviors provide additional important information on the nonisothermal crystallizations of topological PCLs and the resulting crystals as described below.

Foremost, the magnitude of T_{m1} is in the following order: *st*-PCL_{9k} < *l*-PCL_{6k} < *cy*-PCL_{6k} < *cg*-PCL_{9k}. The fact that this trend of T_{m1} resembles that of T_c observed during the first cooling indicates that, for each topological PCLs, the crystallization history is directly reflected in the melting transition. This notion is further supported by the heat of fusion involved in crystal melting peak **1** ($\Delta H_{f,m1}$) and the corresponding crystallinity ($X_{c,m1}$), in which the following trend is established: *st*-PCL_{9k} < *l*-PCL_{6k} < *cg*-PCL_{9k} < *cy*-PCL_{6k}. The increasing trend of $\Delta H_{f,m1}$ and $X_{c,m1}$ resemble those of $\Delta H_{f,c}$ and $X_{c,c}$ obtained from first the cooling. Accordingly, the observed trends on the properties of crystal melting peak **1** reinforces the influence of compact chain conformation induced by cage and cyclic topologies upon enhancing the crystallization of PCL segments.

Crystal melting peak **2** also provides additional evidences that highlight the impact brought by topological influences with some caveat. As for T_{m2} , a predictable increasing trend is determined: $st\text{-PCL}_{9k} < l\text{-PCL}_{6k} < cy\text{-PCL}_{6k} < cg\text{-PCL}_{9k}$. This is the same trend established by T_{m1} and T_c . However, the heat of fusion involved in crystal melting peak **2** ($\Delta H_{f,m2}$) as well as its crystallinity ($X_{c,m2}$), exhibit the increasing order of: $l\text{-PCL}_{6k} < cg\text{-PCL}_{9k} < st\text{-PCL}_{9k} < cy\text{-PCL}_{6k}$. These trends are different from those of $\Delta H_{f,m1}$ and $X_{c,m1}$ as well as $\Delta H_{f,c}$ and $X_{c,c}$. Moreover, $cy\text{-PCL}_{6k}$ reveals larger $\Delta H_{f,m2}$ and higher $X_{c,m2}$ than $cg\text{-PCL}_{9k}$. The relatively lower $\Delta H_{f,m2}$ and smaller $X_{c,m2}$ of $cg\text{-PCL}_{9k}$ may be caused by its bulkier oligonorbonene joints that negatively impact crystallization. Interestingly, $st\text{-PCL}_{9k}$ exhibits larger $\Delta H_{f,m2}$ and higher $X_{c,m2}$ than $cg\text{-PCL}_{9k}$. These rather irregular results may be the outcomes of the competition between the steric influence of the bulky joints and the topological influences. It is hypothesized that such negative steric influence may be minimized by increasing PCL segment length.

The comparison between crystal melting peaks **1** and **2** provides more insights into topological influences. Firstly, the difference between T_{m1} and T_{m2} is in the increasing order: $l\text{-PCL}_{6k} < st\text{-PCL}_{9k} < cg\text{-PCL}_{9k} < cy\text{-PCL}_{6k}$. Secondly, the difference between $\Delta H_{f,m1}$ and $\Delta H_{f,m2}$ is in the decreasing order: $st\text{-PCL}_{9k} > l\text{-PCL}_{6k} \gg cg\text{-PCL}_{9k} > cy\text{-PCL}_{6k}$. For both $l\text{-PCL}_{6k}$ and $cg\text{-PCL}_{9k}$, the $\Delta H_{f,m1}$ values are larger than the $\Delta H_{f,m2}$ values. In contrast, the $\Delta H_{f,m1}$ values of $st\text{-PCL}_{6k}$ and $cy\text{-PCL}_{9k}$ are lower than the $\Delta H_{f,m2}$ values. These trends highlight the positive impact of compact chain conformation and chain end absence on the PCL crystals formed through the nonisothermal crystallization. Furthermore, the total heat of fusions of the crystal meltings ($\Delta H_{f,m}$) as well as the overall crystallinity ($X_{c,m}$) is in the increasing order: $st\text{-PCL}_{9k} < l\text{-PCL}_{6k} < cg\text{-PCL}_{9k} < cy\text{-PCL}_{6k}$. These results collectively inform that the $\Delta H_{f,m}$ and $X_{c,m}$ of PCL are influenced by multiple factors such as topologically influenced chain conformation, the presence or absence of end groups, the bulkiness of chain end groups, and the bulkiness of molecular joints.

Finally, all PCL polymers exhibit single crystallization exothermic peaks during first cooling but two crystal melting endothermic peaks in the subsequent heating, as described above. Here one question arises: why do they all reveal two crystal melting peaks? In the case of $cg\text{-PCL}_{9k}$, slower cooling from the melt state causes higher T_c , consequently leading to higher T_{m1} in the subsequent heating run. Namely, T_c is highly correlated to T_{m1} . In addition, slower cooling rate

causes $\Delta H_{f,m1}$ to increase while $\Delta H_{f,m2}$ decreases. Similar trends are observed for all other counterparts. Interestingly, T_{m2} seems to be independent from the ramping rates in the cooling and heating processes. These results collectively inform the following. The occurrence of T_{m1} (i.e., crystal melting peak **1**) is attributed to the melting phase transition of the PCL crystal domains containing some degree of crystalline defects that quickly formed during the initial cooling process from the melt state, considering the fast kinetic nature of PCL crystallization. The crystal melting peak **2** (i.e., T_{m2}) is assigned to the melting phase transition of the PCL crystal domains exhibiting higher degree of perfectness that occurred during subsequent heating.

Overall, the compact chain conformation and absence of chain ends in *cg*-PCL_{9k} provide significant advantages in the crystallization of PCL segments. Similar outcomes are also observed in the crystallization of *cy*-PCL_{6k}. There is, however, the steric influence of the bulky oligonorbonene joints that slightly diminishes and competes against the topological influences. In contrast, the topology of *st*-PCL_{9k} causes severe demerits in the crystallization in general.

Nanoscale Film Morphologies. Fig. 2a presents a representative of the 2D GISAXS images in scattering angle space measured from nanoscale films (100–120 nm thick) of *cg*-PCL_{9k}. The scattering image reveals a single broad peak positioned along the meridian line and another along the equatorial line; but the scattering intensity is much stronger for the peak along the meridian line. The appearance of such peaks suggests that a mixture of horizontally- and vertically-oriented lamellae is present in the film. Thus, one-dimensional (1D) scattering profiles extracted along the meridian and equatorial lines have been quantitatively analyzed in detail. As displayed in Fig. 2d-e, the extracted 1D scattering profiles are satisfactorily fitted by using the GIXS formula derived with three layer model; the theoretical details regarding the formula is given in the ESI†. Additionally, the secondary orientation factors of the horizontal and vertical lamellae structures have been determined from an azimuthal scattering profile (Fig. 2f) extracted at $q = 0.509 \text{ nm}^{-1}$ from the scattering vector space image (i.e., q -space image) in Fig. 2c. The magnitude of scattering vector q is defined by $q = (4\pi/\lambda)\sin(2\theta/2)$ where 2θ is the scattering angle. All determined structural parameters are summarized in Table 3.

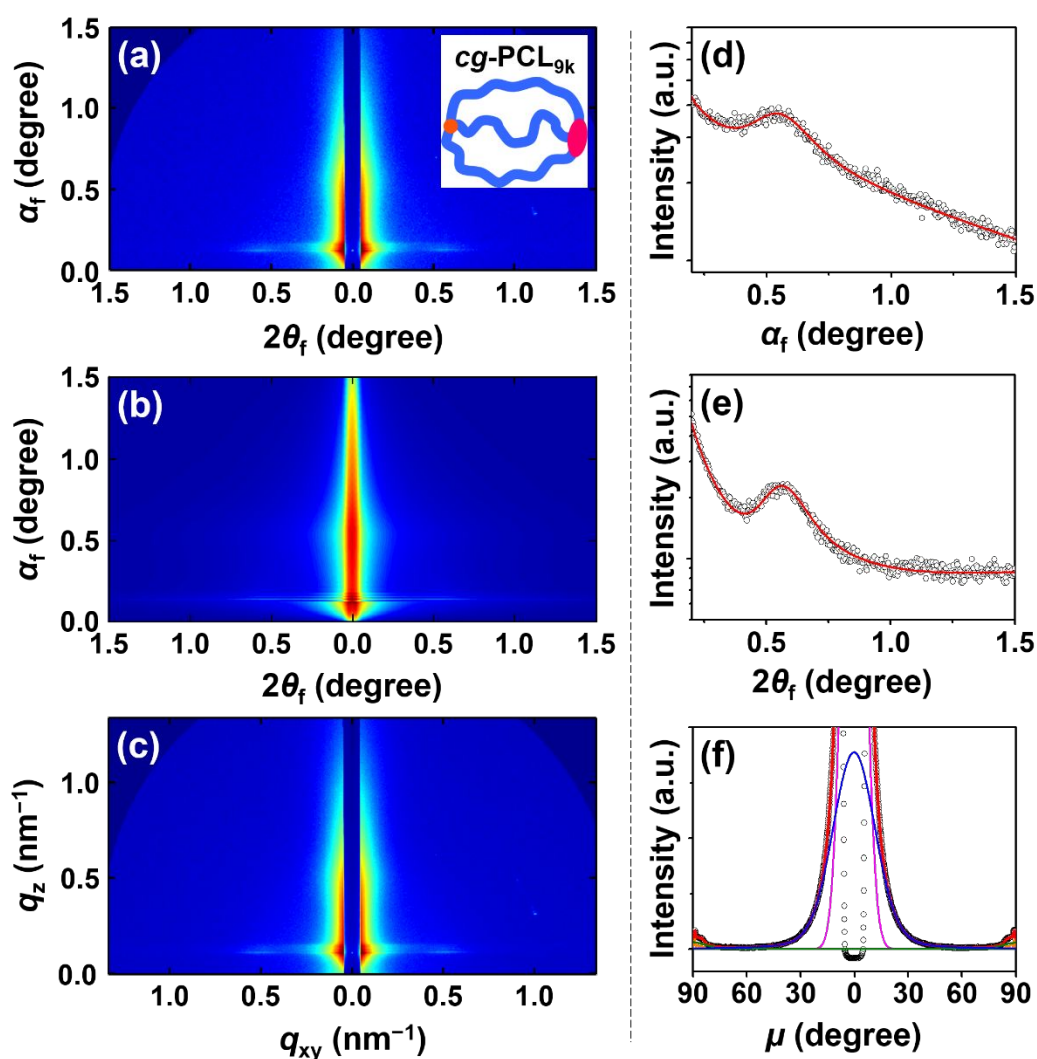


Fig. 2 Representative scattering data of *cg*-PCL_{9k} films (119.5 nm thick) measured with $\alpha_i = 0.1250^\circ$ and SDD = 2926.0 mm at room temperature using a synchrotron X-ray beam ($\lambda = 0.12296$ nm): (a) 2D GISAXS image in scattering angle space; (b) 2D scattering image reconstructed with the determined structural parameters obtained from the analysis of the scattering image in (a); (c) 2D GISAXS image in scattering vector space obtained from the data in (a); (d) out-of-plane scattering profile extracted along the meridian line at $2\theta_f = 0.159^\circ$ from the scattering images in (a); (e) in-plane scattering profile along the equatorial line at $\alpha_f = 0.155^\circ$ from the data in (a); (f) azimuthal scattering profile of the annealed film extracted at $q = 0.509$ nm⁻¹ from the data in (c). In (d) and (e), the open circles represent the measured data and the red solid lines were obtained by fitting the data using the GIXS formula driven with lamellar structure model. In (f), the open circles represent the measured data and the red solid lines represent the sum of horizontal lamella peak (blue line), vertical lamella peaks (green lines), parasitic scattering peak from reflected incident beam (pink line), and Yoneda peaks (orange lines) which were obtained by the deconvolutions of the measured data.

Table 3. Structural parameters of thin film morphologies of topological PCL polymers determined by GISAXS Analysis

Polymer	<i>cg</i> -PCL _{9k}		<i>st</i> -PCL _{9k}		<i>cy</i> -PCL _{6k}	<i>l</i> -PCL _{6k}	
	<i>horizontal</i>	<i>vertical</i>	<i>horizontal</i>	<i>vertical</i>	<i>horizontal</i>	<i>horizontal</i>	<i>vertical</i>
ϕ_L^a (%)	98	2	97	3	100	99	1
L^b (nm)	12.2	11.0	11.9	11.0	11.9	12.4	12.0
l_c^c (nm)	3.1	2.7	2.5	2.3	2.9	2.7	2.5
l_i^d (nm)	3.0	2.8	3.2	3.0	3.0	3.3	3.2
l_a^e (nm)	3.1	2.7	3.0	2.7	3.0	3.1	3.1
σ_c^f (nm)	0.9	0.8	1.0	0.9	0.8	1.1	1.0
σ_i^g (nm)	1.0	1.0	1.3	1.2	0.7	0.9	0.9
g^h	0.23	0.33	0.27	0.35	0.10	0.21	0.38
$\bar{\varphi}_1^i$ (deg.)	0	90	0	89	0	0	88
$\sigma_{\varphi_1}^j$ (deg.)	13.10	7.56	10.80	3.54	10.40	11.60	3.80
$O_{s,1}^k$	0.901	-0.474	0.923	-0.493	0.929	0.907	-0.489

^aVolume fraction of the lamellar structure in either horizontal or vertical orientation determined from azimuthal scattering profiles. ^bLong period of lamellar structure. ^cThickness of the crystalline layer in the phase-separated lamellar structure. ^dThickness of interfacial layer between crystalline and amorphous layers. ^eThickness of the amorphous layer. ^fStandard deviation for the crystalline layer. ^gStandard deviation for the interfacial layer. ^hParacrystal distortion factor along the direction parallel to the long period of lamellar structure. ⁱMean value of the polar angle φ_1 (i.e., orientation angle) between the orientation vector \mathbf{n}_1 (which is set parallel to the axis of the long period of lamellar structure) and the out-of-plane direction of the film (Fig. S1, ESI†). ^jStandard deviation for the orientation angle φ_1 of the lamellar structure. ^kSecond-order orientation factor of lamellar structure.

The quantitative GISAXS analysis confirmed that *cg*-PCL_{9k} forms horizontal lamellar structure as the major structural component (98 vol%) and vertical lamellar structure as the minor component (2 vol%). The horizontal lamella structure has a long period L of 12.4 nm that consists of a crystalline layer l_c of 3.1 nm, two interfacial layers l_i of 6.0 nm ($l_i = 3.0$ nm), and an amorphous layer l_a of 3.1 nm. In addition, it is characterized by the lattice distortion factor g of 0.23, and the second-order orientation factor $O_{s,1}$ of 0.901 ($\bar{\varphi}_1 = 0^\circ$, mean polar angle between the orientation

vector \mathbf{n}_1 parallel to the axis of L and the out-of-plane direction of the film; $\sigma_{\phi_1} = 13.10^\circ$, standard deviation of polar angle ϕ_1 (Fig. S1, ESI†)). Compared to the horizontal lamellar structure, the vertical lamellar structure is defined by slightly shorter structural parameters and a larger g -factor (i.e., higher lattice distortion). However, the vertical lamellar structure exhibits a slightly better orientation with $O_{s,1}$ value of -0.474 . With the determined structural parameters, a 2D scattering image has been reconstructed using the GIXS formula, as shown in Fig. 2b. The reconstructed image is in good agreement with the measured scattering pattern, which confirms that the scattering data have been analyzed successfully.

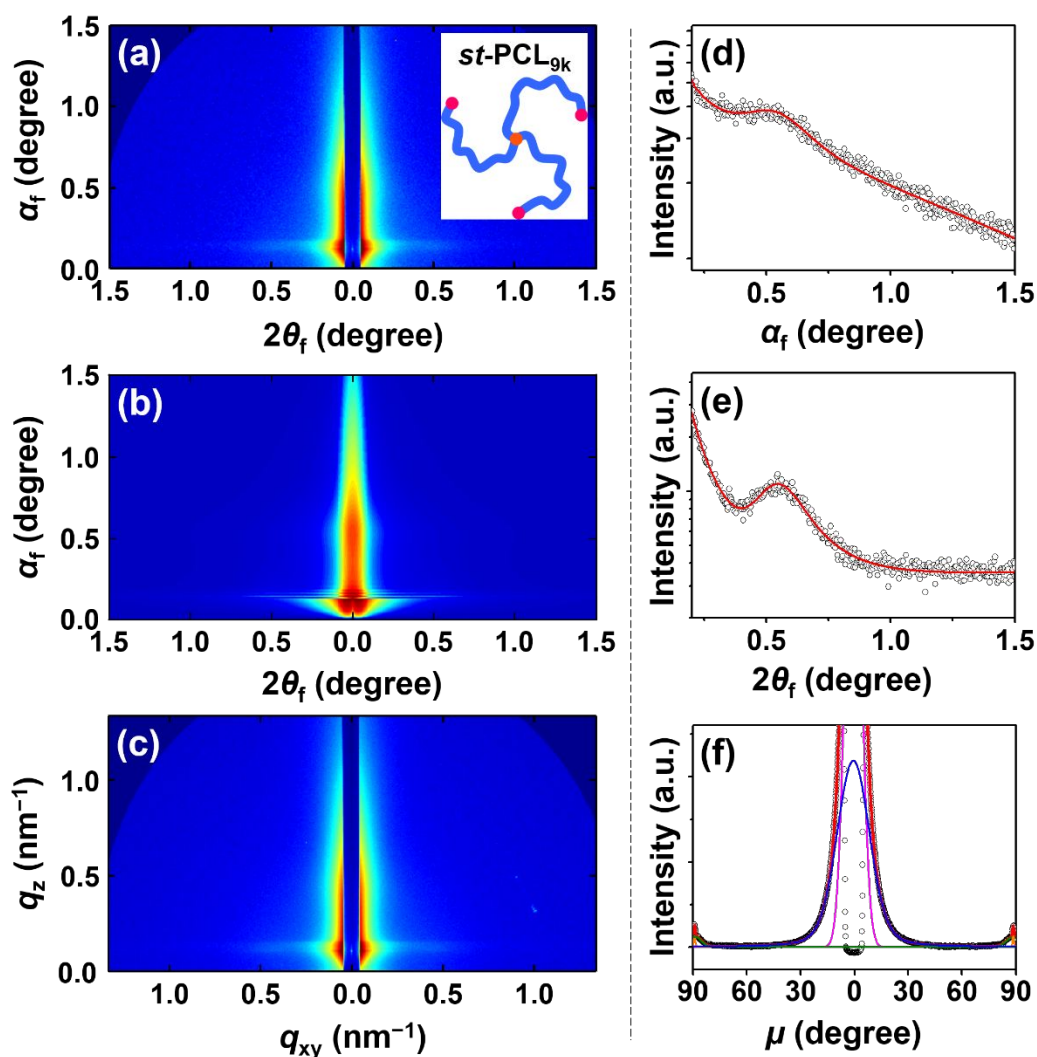


Fig. 3 Representative scattering data of *st*-PCL_{9k} films (105.3 nm thick) measured with $\alpha_i = 0.1240^\circ$ and SDD = 2926.0 mm at room temperature using a synchrotron X-ray beam ($\lambda = 0.12296$

nm): (a) 2D GISAXS image in scattering angle space; (b) 2D scattering image reconstructed with the determined structural parameters obtained from the analysis of the scattering image in (a); (c) 2D GISAXS image in scattering vector space obtained from the data in (a); (d) out-of-plane scattering profile extracted along the meridian line at $2\theta_f = 0.159^\circ$ from the data in (a); (e) in-plane scattering profile along the equatorial line at $\alpha_f = 0.135^\circ$ from the data in (a); (f) azimuthal scattering profile extracted at $q = 0.511 \text{ nm}^{-1}$ from the data in (c). In (d) and (e), the open circles represent the measured data and the red solid lines were obtained by fitting the data using the GIXS formula driven with lamellar structure model. In (f), the open circles represent the measured data and the red solid lines represent the sum of horizontal lamella peak (blue line), vertical lamella peaks (green lines), parasitic scattering peak from reflected incident beam (pink line), and Yoneda peaks (orange lines) which were obtained by the deconvolutions of the measured data.

Fig. 3 presents a representative GISAXS image in scattering angle space of *st*-PCL_{9k} films (100–120 nm thick). The 2D scattering pattern resembles that of the *cg*-PCL_{9k} film. Its out-of-plane and in-plane 1D scattering profiles are also satisfactorily fitted by using the GIXS formula of lamellar structural model (Fig. 3d-e). An azimuthal scattering profile, which has been extracted at $q = 0.511 \text{ nm}^{-1}$ from the q -space image, is analyzed in detail, as displayed in (Fig. 3f). The analysis results are compared with those of the *cg*-PCL_{9k} film in Table 3. The 2D scattering image, which has been reconstructed with the determined structural parameters, is consistent with the measured data, confirming that the scattering data analysis has been done successfully (Fig. 3a,b).

The analysis confirms the formation of a mixture of horizontal and vertical lamellae domains made by *st*-PCL_{9k}, similar to *cg*-PCL_{9k}. The volume fractions of horizontal and vertical lamellae are 97 % and 3 %, respectively; here, it is noted that the vertical structure is found to be tilted by 1° from the out-of-plane direction of the film. The horizontal lamella shows slightly longer structural parameters (L , l_c , l_i , and l_a), higher orientational distribution, and less lamellar lattice distortion than the vertical lamella. When compared against *cg*-PCL_{9k}, *st*-PCL_{9k} forms a more compact horizontal lamella with shorter L , l_c , and l_a , and longer l_i . Also, it exhibits a higher level of lattice distortion and a lower orientational distribution.

Similar scattering images have been measured for the nanoscale films (96–120 nm thick) of *cy*-PCL_{6k} and *l*-PCL_{6k} (Fig. 4a and 5a). They have been quantitatively analyzed in the same manner

as done for those of the *cg*-PCL_{9k} and *st*-PCL_{9k} films (Fig. 4b-f and 5b-f). The analysis results are summarized in Table 3.

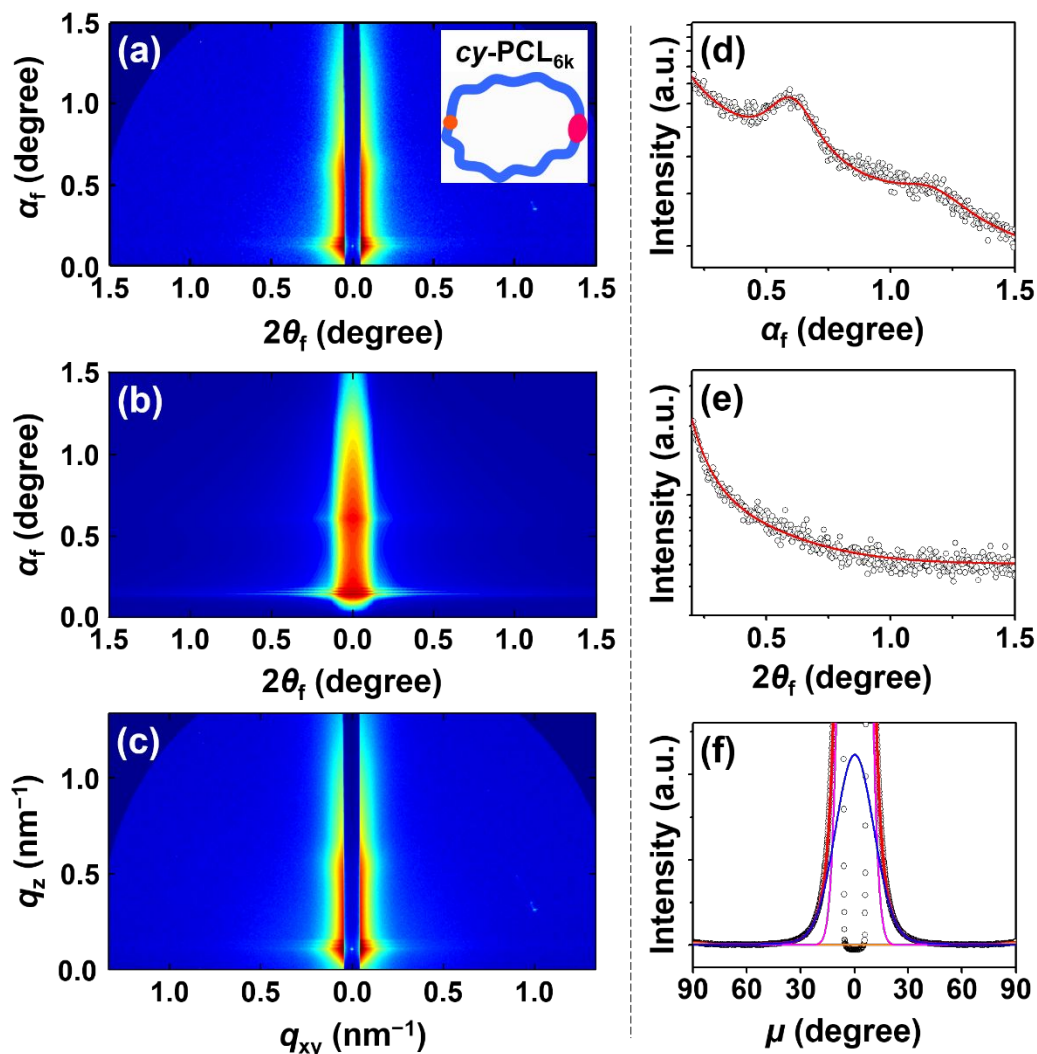


Fig. 4 Representative scattering data of *cy*-PCL_{6k} films (115.8 nm thick) measured with $\alpha_i = 0.1240^\circ$ and SDD = 2926.0 mm at room temperature using a synchrotron X-ray beam ($\lambda = 0.12296$ nm): (a) 2D GISAXS image in scattering angle space; (b) 2D scattering image reconstructed with the determined structural parameters obtained from the analysis of the data in (a); (c) 2D GISAXS image in scattering vector space obtained from the data in (a); (d) out-of-plane scattering profile extracted along the meridian line at $2\theta_f = 0.159^\circ$ from the data in (a); (e) in-plane scattering profile along the equatorial line at $\alpha_f = 0.201^\circ$ from the data in (a); (f) azimuthal scattering profile extracted at $q = 0.548$ nm⁻¹ from the data in (c). In (d) and (e), the open circles represent the measured data and the red solid lines were obtained by fitting the data using the GIXS formula driven with lamellar structure model. In (f), the open circles represent the measured data and the red solid lines represent the sum of horizontal lamella peak (blue line), vertical lamella peaks (green lines), parasitic scattering peak from reflected incident beam (pink line), and Yoneda peaks (orange lines) which were obtained by the deconvolutions of the measured data.

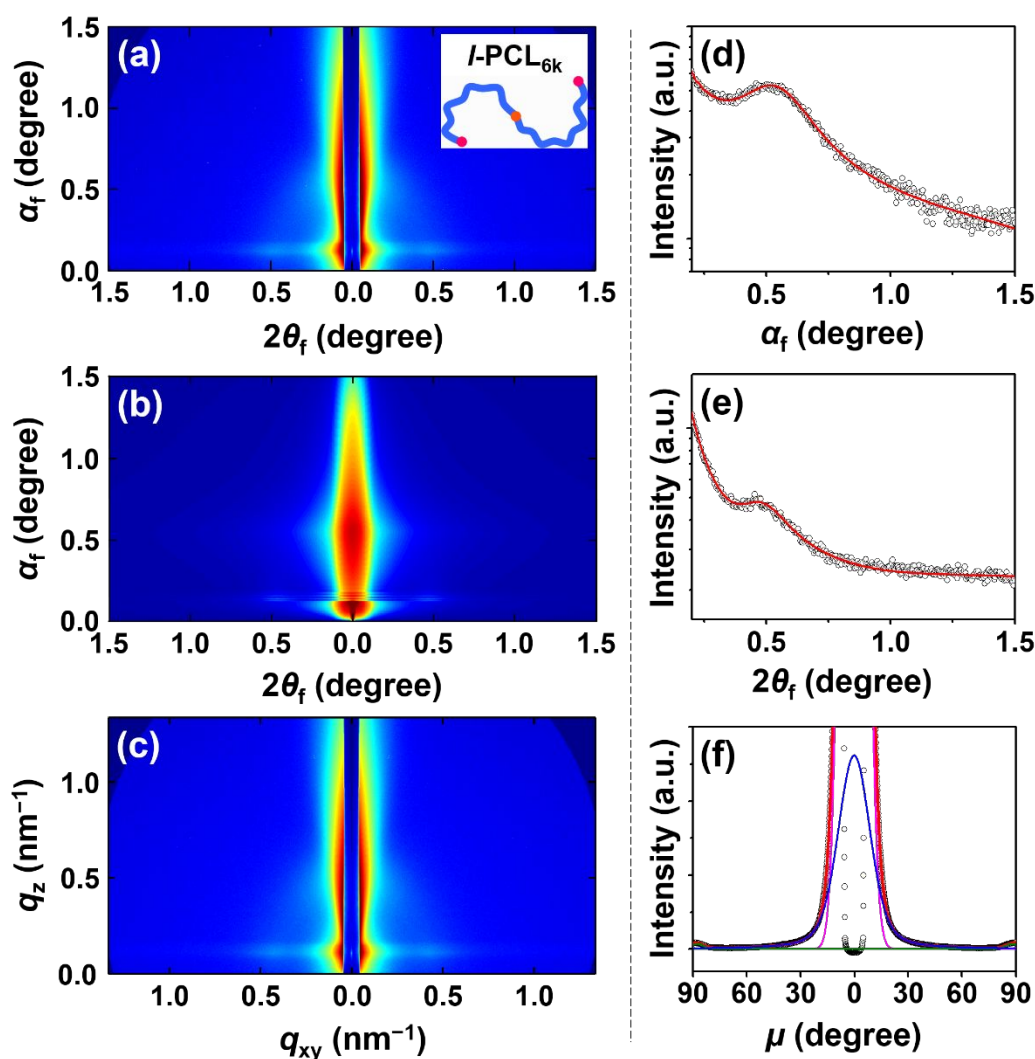


Fig. 5 Representative scattering data of *l*-PCL_{6k} films (96.0 nm thick) measured with $\alpha_i = 0.1190^\circ$ and SDD = 2954.0 mm at room temperature using a synchrotron X-ray beam ($\lambda = 0.12357$ nm): (a) 2D GISAXS image in scattering angle space; (b) 2D scattering image reconstructed with the determined structural parameters obtained from the analysis of the data in (a); (c) 2D GISAXS image in scattering vector space obtained from the data in (a); (d) out-of-plane scattering profile extracted along the meridian line at $2\theta_f = 0.202^\circ$ from the data in (a); (e) in-plane scattering profile along the equatorial line at $\alpha_f = 0.133^\circ$ from the data in (a); (f) azimuthal scattering profile extracted at $q = 0.421$ nm⁻¹ from the data in (c). In (d) and (e), the open circles represent the measured data and the red solid lines were obtained by fitting the data using the GIXS formula driven with lamellar structure model. In (f), the open circles represent the measured data and the red solid lines represent the sum of horizontal lamella peak (blue line), vertical lamella peaks (green lines), parasitic scattering peak from reflected incident beam (pink line), and Yoneda peaks (orange lines) which were obtained by the deconvolutions of the measured data.

Interestingly, *cy*-PCL_{6k} exclusively forms horizontal lamellar structure. In comparison to *cg*-PCL_{9k}, *cy*-PCL_{6k} forms horizontal lamella with slightly shorter long period and thinner crystalline and amorphous layers. Moreover, the lamellar structure additionally exhibits a lower lattice distortion ($g = 0.10$) and an improved horizontal orientation ($O_{s,1} = 0.929$) than those of the cage-

shaped counterpart. In contrast, *l*-PCL_{6k} exhibits a mixture of horizontal (99 %) and vertical (1 %) lamellar structures, as similarly observed in *cg*-PCL_{9k} film. Overall, the horizontal lamella exhibits less lattice distortion and longer structural parameters than those of the vertical lamella, except for the amorphous layer thickness that turns out to be identical in the two domains. However, the orientational distribution is lesser for the vertical structure. Here, the vertical structure is found to be tilted by 2° from the out-of-plane direction of the film. When compared against *cy*-PCL_{6k}, *l*-PCL_{6k} forms horizontal lamella with longer *L*, thicker interfacial and amorphous layers, as well as a lesser orientation order (i.e., larger orientation distribution) and thinner crystalline layer. In addition, it reveals a longer *L*, a thicker interfacial layer and a better orientation order, but a thinner crystalline layer in comparison to the horizontal lamella in the *cg*-PCL_{9k} film.

The nanoscale PCL films have been further investigated via GIWAXS. A representative 2D GIWAXS image in scattering angle space of the *cg*-PCL_{9k} film is presented in Fig. 6a; its *q*-space image is shown in Fig. 6c. The image shows several scattering peaks. PCL is known to form laterally-packed crystals in orthorhombic lattice with a space group of *P*2₁2₁2₁ (3D representation shown in Fig. S2a, ESI†).^{36,37} Taking this orthorhombic lattice unit into account, the following peaks have been identified and indexed: {002}, {004}, {110}, {102}, and {200}. Based on these reflection peaks, the lattice dimension parameters are determined: *a* = 0.805 nm, *b* = 0.556 nm, and *c* = 1.754 nm. In particular, the {110} reflection appears around $2\theta_f = 15.8^\circ$ ($q_{xy} = 14.2 \text{ nm}^{-1}$) as the strongest peak along the equatorial line at $\alpha_f = 0^\circ$, indicating that the majority of orthorhombic PCL crystal lattices (i.e., the *c*-axis of the lattices parallel to the extended PCL chain units accommodated in the crystal lattice) is oriented vertically (Fig. S2, ESI†). Interestingly, another {110} reflection is observed around $2\theta_f = 13.7^\circ$ and $\alpha_f = 9.3^\circ$ as a relatively weaker spot. Furthermore, a {200} reflection appears at $\alpha_f = 17.4^\circ$ and $2\theta_f = 0^\circ$, which is orthogonal to the {200} reflection of aforementioned vertically-oriented PCL crystal. These two reflections

originate from horizontally-oriented PCL crystal residing within the vertical lamellar structure. Considering the GISAXS results showing that vertical lamellar structure exists as the minor portion (Table 3), the relatively weaker $\{110\}$ and $\{200\}$ reflection peaks are indeed originating from horizontally-oriented crystal lattice.

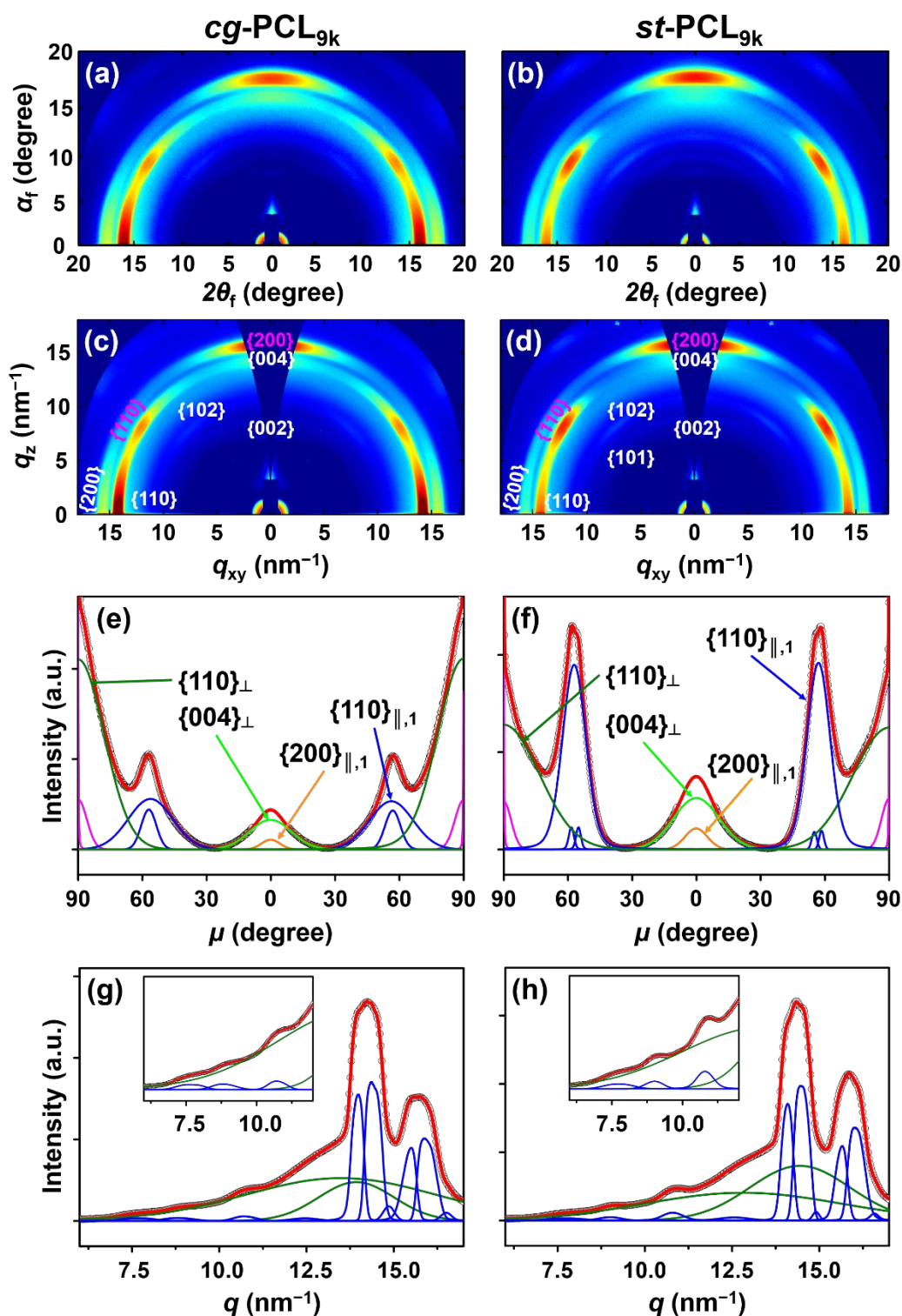


Fig. 6 Representative GIWAXS data of *cg*-PCL_{9k} and *st*-PCL_{9k} films measured with SDD = 210.9 mm at room temperature using a synchrotron X-ray beam ($\lambda = 0.12296$ nm): (a) 2D image in scattering angle space of *cg*-PCL_{9k} (119.5 nm thick; $\alpha_i = 0.1340^\circ$); (b) 2D image in scattering angle space of *st*-PCL_{9k} (105.3 nm thick; $\alpha_i = 0.1560^\circ$); (c) 2D image in scattering vector q space of *cg*-PCL_{9k} obtained from the data in (a); (d) 2D image in scattering vector q space of *st*-PCL_{9k} obtained from the data in (b); (e) azimuthal scattering profile extracted at $q = 14.2$ nm⁻¹ from the data in (c); (f) azimuthal scattering profile extracted at $q = 14.2$ nm⁻¹ from the data in (d); (g) 1D scattering profile averaged quadrantly from the scattering image in (c); (h) 1D scattering profile averaged quadrantly from the scattering image in (d). In (c) and (d), peaks from vertically-oriented crystals are indexed in white font, and peaks from horizontally-oriented crystals (in which the {100} plane

of orthorhombic lattice is parallel to the film plane) are indexed in pink font. In (e) and (f), the open circles represent the measured data and the red solid lines represent the sum of the {110} peak of vertically-oriented crystals (dark green lines), the {110} peak of horizontally-oriented crystals (blue lines), the {004} peak of vertically-oriented crystals (light green line), the {200} peak of horizontally-oriented crystals (orange line), and Yoneda peaks (pink lines) which were obtained by the deconvolutions of the measured data. “ \perp ” and “ \parallel ” subscripts denote the peaks from vertically-oriented crystals and horizontally-oriented crystals, respectively. In (g) and (h), the open circles represent the measured data and the red solid lines represent the sum of crystal peaks (blue lines), and amorphous peaks (green lines).

With these information, an azimuthal scattering profile is extracted at $q = 14.2 \text{ nm}^{-1}$ (at which the {110} reflections appear) from the q -space image in Fig. 6c as a function of azimuthal angle μ . Deconvolution of scattering peaks (Fig. 6e) has identified the {110} reflection peak to appear at $\mu = 90.0^\circ$ and 56.3° ; the relative area ratios of the two peaks are 77.6 % and 22.4 % respectively. The deconvolution results confirm the entire PCL crystallites in the cg -PCL_{9k} film are composed of vertically-oriented (77.6 %), and horizontally-oriented (22.4 %) orthorhombic crystals with respect to the film plane. Considering $\mu = 56.3^\circ$ for the {110} reflection from horizontally-oriented crystal, the {100} plane of its orthorhombic lattice is set parallel to the film plane. Among these crystal lattices, the vertical crystal lattice (the major crystal lattice component) is estimated to have a second-order orientation factor $O_{s,2}$ of 0.917 ($\bar{\varphi}_2 = 90^\circ$, mean value of the polar angle φ_2 between the orientation vector \mathbf{n}_2 set parallel to the c -axis of the orthorhombic PCL crystal lattice and the out-of-plane direction of the film; $\sigma_{\varphi_2} = 12.48^\circ$, standard deviation for the orientation angle φ_2 (Fig. S2, ESI[†])). In addition, the overall crystallinity $X_{c,GIWAXS}$ is estimated to be 38.4 % by analyzing the 1D scattering profile averaged quadrantly from the q -space scattering image (Fig. 6g). The {110} and {200} reflection peaks have been fitted with multiple functions to account for the peak broadening apparent in the data. The analysis results are summarized in Table 4.

Table 4. Orientations and Structural Parameters of PCL Crystallites in Thin Film Determined by Quantitative GIWAXS Analysis

Polymer	<i>cg</i> -PCL _{9k}	<i>st</i> -PCL _{9k}	<i>cγ</i> -PCL _{6k}	<i>l</i> -PCL _{6k}
<i>Crystallite orientation</i>				
Vertical ^a (%)	77.6 (90.0°) ^l	64.8 (90.0°)	98.6 (90.0°)	85.2 (90.0°)
Horizontal _{100} ^b (%)	22.4 (56.3°)	35.2 (57.1°)	--	12.3 (58.3°)
Horizontal _{110} ^c (%)	--	--	1.4 (69.6°) ^m	2.5 (70.7°) ^m
<i>Overall crystallinity</i>				
<i>X</i> _{c,GIWAXS} ^d (%)	38.4	36.7	39.7	31.8
<i>Structural parameters</i> ^e				
<i>a</i> ^f (nm)	0.805	0.800	0.794	0.794
<i>b</i> ^g (nm)	0.556	0.551	0.551	0.521
<i>c</i> ^h (nm)	1.754	1.753	1.705	1.699
$\bar{\varphi}_2$ ⁱ (deg.)	0	0	0	0
σ_{φ_2} ^j (deg.)	12.48	16.93	9.08	13.72
<i>O</i> _{s,2} ^k	0.917	0.879	0.944	0.915

^aFraction in percentage of PCL crystallites oriented vertically with respect to the film plane. ^bFraction in percentage of horizontally-oriented PCL crystallites in which the {100} plane of orthorhombic lattice is parallel to the film plane. ^cFraction in percentage of horizontally-oriented PCL crystallites in which the {110} plane of orthorhombic lattice is parallel to the film plane. ^dCrystallinity determined from the whole oriented crystallites. ^eDetermined from the vertically-oriented PCL crystallites. ^fUnit cell dimension along the *a*-axis of orthorhombic PCL crystallite. ^gUnit cell dimension along the *b*-axis of orthorhombic PCL crystallite. ^hUnit cell dimension along the *c*-axis of orthorhombic PCL crystallite. ⁱMean value of the polar angle φ_2 (i.e., orientation angle) between the orientation vector \mathbf{n}_2 (which is set parallel to the *c*-axis of the PCL crystallite) and the out-of-plane direction of the film (Fig. S2, ESI[†]). ^jStandard deviation for the orientation angle φ_2 of the PCL crystallite. ^kSecond-order orientation factor. ^lAzimuthal angle of {110} reflections of PCL crystallites with respect to the film plane. ^mAzimuthal angle of $\bar{1}10$ reflection of PCL crystallites with respect to the film plane.

Similar GIWAXS images are observed for the nanoscale films the nanoscale films of all counterparts. As shown in Fig. 6b,d,f,h and 7a-h, the scattering data are analyzed in the same manner as for the *cg*-PCL_{9k} film. All analysis results are summarized in Table 4. Star, cyclic, and linear counterparts exhibit crystal lattice dimensions nearly identical to those of *cg*-PCL_{9k}. However, the individual counterparts reveal some differences regarding the orientations of PCL crystallites and overall crystallinities depending on the molecular topologies.

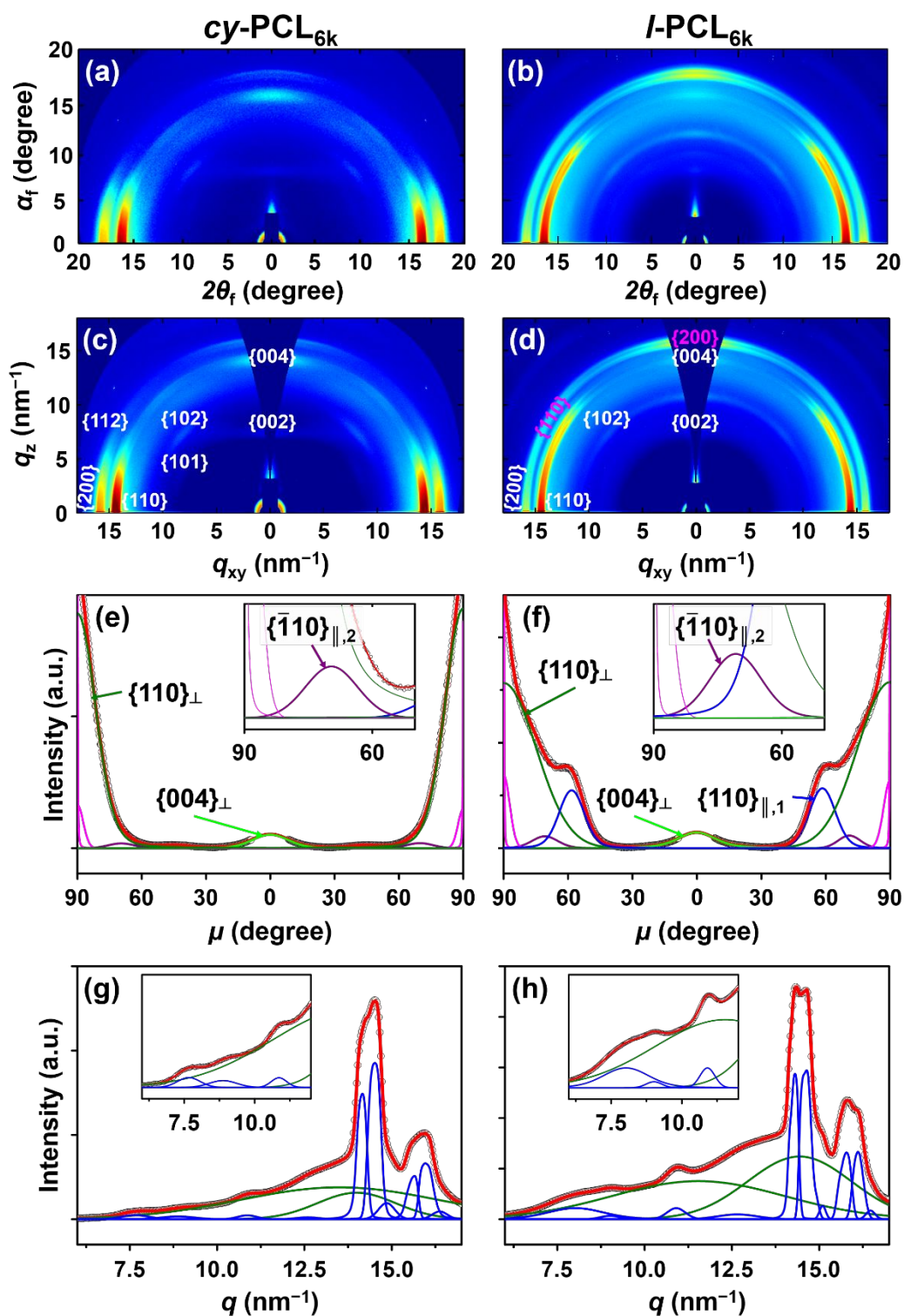


Fig. 7 Representative GIWAXS data of *cy*-PCL_{6k} and *l*-PCL_{6k} films measured at room temperature using a synchrotron X-ray beams: (a) 2D image in scattering angle space of *cy*-PCL_{6k} film (115.8 nm thick; $\alpha_i = 0.1450^\circ$; $\lambda = 0.12296$ nm; SDD = 210.9 mm); (b) 2D image in scattering angle space of *l*-PCL_{6k} film (96.0 nm thick; $\alpha_i = 0.1620^\circ$; $\lambda = 0.12357$ nm; SDD = 209.9 mm); (c) 2D image in scattering vector q space obtained from the data in (a); (d) 2D image in scattering vector q space obtained from the data in (b); (e) azimuthal scattering profile extracted at $q = 14.2$ nm⁻¹ from the data in (c); (f) azimuthal scattering profile extracted at $q = 14.2$ nm⁻¹ from the data in (d); (g) 1D scattering profile averaged quadrantally from the data in (c); (h) 1D scattering profile averaged quadrantally from the data in (d). In (c) and (d), peaks from vertically-oriented crystals are indexed in white font, and peaks from horizontally-oriented crystals (in which the {100} plane of

orthorhombic lattice is parallel to the film plane) are indexed in pink font. In (e) and (f), the open circles represent the measured data and the red solid lines represent the sum of the $\{110\}$ peak of vertically-oriented crystals (green lines), the $\{110\}$ peak of horizontally-oriented crystal with the $\{100\}$ plane of orthorhombic lattice set parallel to the film plane (blue lines), the $\{004\}$ peak of vertically-oriented crystals (light green line), the $\{110\}$ peak of horizontally-oriented crystal with the $\{100\}$ plane of orthorhombic lattice set parallel to the film plane (purple lines), and Yoneda peaks (pink lines) which were obtained by the deconvolutions of the measured data. “ \perp ”, “ $\parallel,1$ ” and “ $\parallel,2$ ” subscripts denote the peaks from vertically-oriented crystals, horizontally-oriented crystals with the $\{100\}$ plane of orthorhombic lattice set parallel to the film plane, and horizontally-oriented crystals with the $\{110\}$ plane of orthorhombic lattice set parallel to the film plane, respectively. In (g) and (h), the open circles represent the measured data and the red solid lines represent the sum of crystal peaks (blue lines), and amorphous peaks (green lines).

The GISAXS and GIWAXS analyses collectively provide key information on how the molecular topologies make impacts on the nanoscale morphology of PCL, as described below. In addition, the analysis results also reflect on the impacts brought by sterics of molecular joints and chain end groups upon the structural characteristics of PCL film. First of all, PCL consistently forms lamellar structures composed of crystalline layers and amorphous layers regardless of the molecular topologies. The strong tendency to form lamellar crystals could originate from the thermodynamically favorable self-assembling ability of PCL chains (i.e., crystallization). Moreover, *cg*-PCL_{9k}, *st*-PCL_{9k}, and *l*-PCL_{6k} form lamellar structure with mixed orientation, where the horizontal lamella is the major structural component (97–99 %) and the vertical lamella is the minor component (1–3 vol%). This leaves *cy*-PCL_{6k} as the only polymer to form unidirectional, horizontal lamellar structure. Interestingly, *cy*-PCL_{6k} once again stands out from the other polymers in the formation of horizontal lamellar structure when listing the increasing trends over the levels of lattice distortion g (*cy*-PCL_{6k} < *l*-PCL_{6k} < *cg*-PCL_{9k} < *st*-PCL_{9k}), and second-order orientation factor of lamellar structure $O_{s,1}$ (*cg*-PCL_{9k} < *l*-PCL_{6k} < *st*-PCL_{9k} < *cy*-PCL_{6k}). This confirms that, in this study, the cyclic topology succeeds in enhancing the self-assembly of PCL by forming unidirectional horizontal lamella with high orientation order while maintaining the highest structural order. As for other topology types, additional structural parameters have to be evaluated in conjunction to precisely identify their merits or demerits.

While the long periods of lamellar structures can be listed in the increasing order of $st\text{-PCL}_{9k} \sim cy\text{-PCL}_{6k} < cg\text{-PCL}_{9k} < l\text{-PCL}_{6k}$, the crystalline layer thickness of lamellar structure is in the increasing order: $st\text{-PCL}_{9k} < l\text{-PCL}_{6k} < cy\text{-PCL}_{6k} < cg\text{-PCL}_{9k}$. It is generally known that thicker crystal exhibits higher T_m and this correlation is confirmed when comparing with the DSC results. Furthermore, the interfacial layer thickness is in the increasing order of $cg\text{-PCL}_{9k} \sim cy\text{-PCL}_{6k} < st\text{-PCL}_{9k} < l\text{-PCL}_{6k}$, and the amorphous layer thickness is listed in increasing order: $l\text{-PCL}_{6k} \sim cg\text{-PCL}_{9k} < st\text{-PCL}_{9k} \sim cy\text{-PCL}_{6k}$. Considering the formation of crystalline layers based on the orthorhombic lattice units, the presence of chain end groups increasing the degree of freedom on chain conformations would diminish the crystalline layer and consequently increase the thickness of the interfacial and amorphous layers. Between $cg\text{-PCL}_{9k}$ and $cy\text{-PCL}_{6k}$, it is theorized that cage topology is more advantageous in forming thicker crystalline layer by having one more PCL segment within the compact chain conformation than cyclic topology, although the difference in l_c is fairly small.

Inside the crystalline layer, all PCL polymers favorably form orthorhombic crystal lattices as the crystalline layer component in the lamellar structure, regardless of the topologies: $a = 0.790 \sim 0.805$ nm, $b = 0.548 \sim 0.556$ nm, $c = 1.701 \sim 1.754$ nm, and $\alpha = \beta = \gamma = 90^\circ$. Here, the c value corresponds to the length of two repeat units plus one carbonyl carbon atom in a fully extended chain conformation. The orthorhombic crystal lattice present in the lamellar structure, however, reveals varying ratios between vertical and horizontal orientations. Both $st\text{-PCL}_{9k}$ and $l\text{-PCL}_{6k}$ also possess the horizontally-oriented crystals found in $cg\text{-PCL}_{9k}$ evidenced by the $\{110\}$ reflection occurring at $\mu = 57.1^\circ$ and 58.3° (Fig. 6f and 7f), respectively. Interestingly, $l\text{-PCL}_{6k}$ reveals another reflection at $\mu = 70.7^\circ$ with a relative fraction of 2.5 %. Considering the μ value, this particular reflection is likely the $\{\bar{1}10\}$ reflection originating from a secondary horizontally-oriented crystal where its $\{110\}$ plane is parallel to the film plane. This particular reflection is also found in $cy\text{-PCL}_{6k}$ with a relative fraction of 1.4 % (Fig. 6e, Table 4). Interestingly, $cy\text{-PCL}_{6k}$ does

not reveal any signals from horizontally-oriented crystals with the $\{100\}$ plane set parallel to the film.

Among these domains, the vertically-oriented crystal lattice domain is dominant for all topological polymer films. Overall, the relative fractions of vertically-oriented PCL crystals reveal an increasing trend as following: $st\text{-PCL}_{9k} < cg\text{-PCL}_{9k} < l\text{-PCL}_{6k} < cy\text{-PCL}_{6k}$. Surprisingly, This trend matches the volume fractions of the horizontal lamellar structures characterized from GISAXS data: $st\text{-PCL}_{9k} < cg\text{-PCL}_{9k} < l\text{-PCL}_{6k} < cy\text{-PCL}_{6k}$. The $O_{s,2}$ value (i.e., second-order orientation factor) of vertically-oriented orthorhombic crystal lattices in the lamellar structure is in the increasing order: $st\text{-PCL}_{9k} < l\text{-PCL}_{6k} < cg\text{-PCL}_{9k} < cy\text{-PCL}_{6k}$. It is critical to note that, despite being theorized to be advantageous for crystalline layer formation, cage topology presents less orientation order than cyclic topology. At this point, there seems to be an opposing competition between the influences from compact chain conformation and steric hindrance of oligonorbonene joints. By having a larger molecular joint, cage topology seems to suffer a reduced control of the orientation order of the PCL crystals when compared to cyclic topology. As for star topology, one could easily expect the lowest orientation order due the highest number of chain ends amongst the subjects of this study. The negative impact of sterics can also be observed by listing the overall crystallinity in the increasing order: $l\text{-PCL}_{6k} < st\text{-PCL}_{9k} < cg\text{-PCL}_{9k} < cy\text{-PCL}_{6k}$.

All determined film morphologies are schematically depicted in Fig. 8. Overall, all topological PCL polymers reveal to form lamellar structures based on orthorhombic crystal lattice. The structural parameters including overall crystallinity and orientational orthorhombic crystal domains are, however, influenced by the molecular topologies. Furthermore, the sterics of molecular joints and chain end groups compete against the topological effects producing varying degrees of outcome upon multiple structural parameters of the self-assembled structures of PCL.

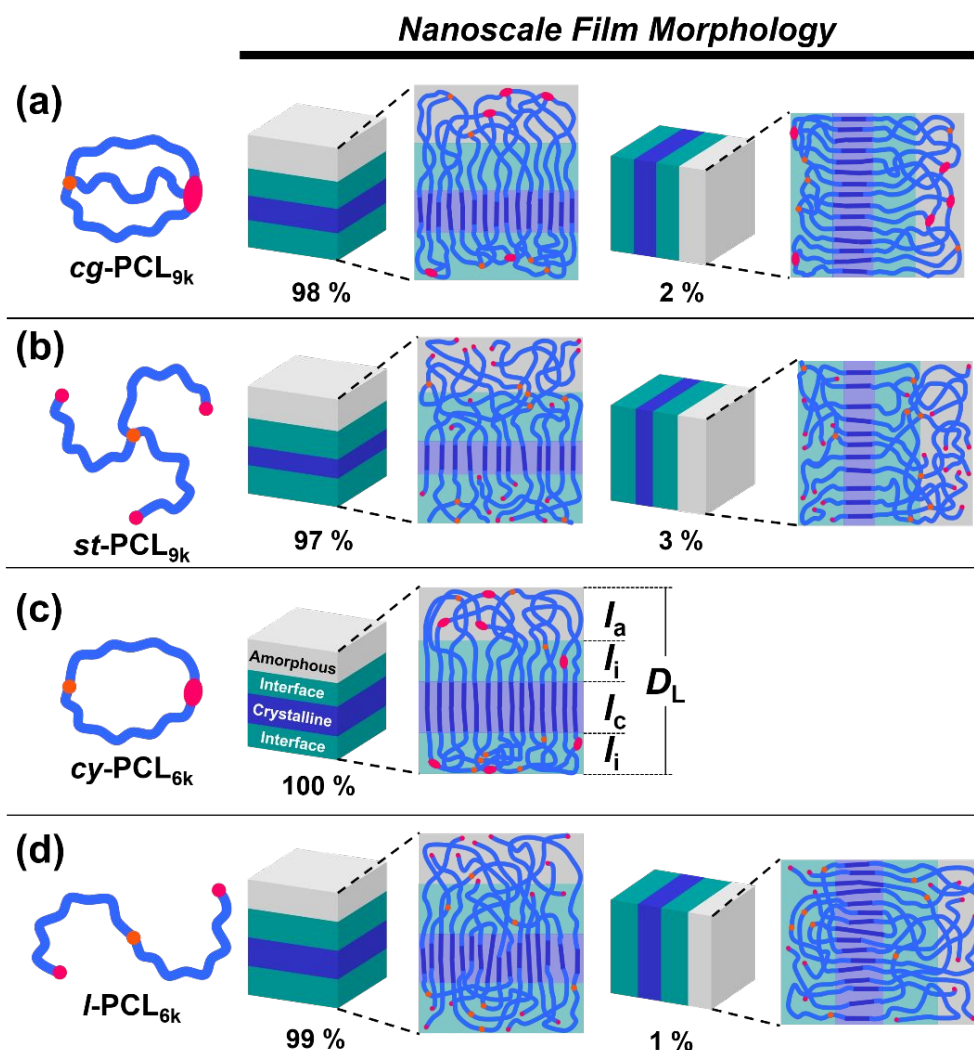


Fig. 8 Schematic representations of molecular chain conformations and packing orders in the nanoscale films of various topological PCL polymers.

Conclusions

In this study, a cage-shaped PCL polymer and its various topological counterparts in bulk states have been examined in terms of thermal stability and phase transitions. The nanoscale film morphologies of the topological PCL polymers have been investigated quantitatively by synchrotron GIXS analyses.

The PCL polymers show topology and end group dependent thermal stabilities; $T_{d,5}$: l -PCL_{6k} < cg -PCL_{9k} \sim cy -PCL_{6k} \sim st -PCL_{9k}. These results confirm that both cage-shaped and cyclic topologies benefit from their topology types to achieve higher thermal stability of PCL. Moreover,

the influence of topological effect is clearly demonstrated in the crystallization temperature and crystal melting temperature of PCL. For $T_{c,max}$, T_{m1} and T_{m2} , the topological polymers follow the trend of: $st\text{-PCL}_{9k} < l\text{-PCL}_{6k} < cy\text{-PCL}_{6k} < cg\text{-PCL}_{9k}$. The other phase transition characteristics (heat of crystallization, heat of fusion, and crystallinity) exhibit a more intricate dependency on both the molecular topologies as well as steric influences from the molecular joints and end groups.

In nanoscale films, all PCL homopolymers always form lamellar structures based on orthorhombic crystal lattice. Amongst the lamellar structural parameters, the crystalline layer thickness l_c shows a clear evidence of the topological influence effect with the following trend: $st\text{-PCL}_{9k} < l\text{-PCL}_{6k} < cy\text{-PCL}_{6k} < cg\text{-PCL}_{9k}$. Other structural characteristics such as compositional ratio amongst crystalline interfacial, and amorphous layers, crystallinity, and the orientation of orthorhombic lattice, however, once again exhibit a rather complex correlation to topological and steric influences.

Overall, this study's evaluation of cage topology in conjunction with the respective cyclic, star, and linear analogues demonstrates that the self-assembly characteristics of PCL is rather critically affected by the opposing competition between the topological and steric influences. Additionally, this indicates that the morphological behaviors of highly complex topological polymers such as cage-shaped polymers are far more sophisticated than theorizing them as simplified geometrical objects, and the chemical structures of molecular joints must be critically contemplated in the synthesis to maximize the beneficial topological influences to self-assembly behaviors of polymers.

Conflicts of Interest

The authors declare no conflict of interest.

Acknowledgements

This study was supported from JSPS Grant-in-Aid for Scientific Research (A and B) (19H00905 and 19H02769, T.S.), JSPS Grant-in-Aid for Challenging Exploratory Research (19K22209, T.S.), JST CREST (JPMJCR19T4, T.S.), the Photoexcitonix Project (Hokkaido University, T.S.), Creative Research Institute (CRIS, Hokkaido University, T. S.) and the Frontier Chemistry Center (Hokkaido University, T.S., T.I., and B.J.R.). B.J.R. and Y.M. were funded by the JSPS Fellowship for Young Scientists. The authors thank the Pohang Accelerator Laboratory for providing opportunities to conduct synchrotron X-ray scattering measurements.

References

- (1) S. Juul, F. Iacovelli, M. Falconi, S. L. Kragh, B. Christensen, R. Frøhlich, O. Franch, E. L. Kristoffersen, M. Stougaard, K. W. Leong, Y. P. Ho, E. S. Sørensen, V. Birkedal, A. Desideri and B. R. Knudsen, *ACS Nano*, 2013, **7**, 9724–9734.
- (2) M. Yoshizawa, J. K. Klosterman and M. Fujita, *Angew. Chem. Int. Ed.*, 2009, **48**, 3418–3438.
- (3) R. McCaffrey, H. Long, Y. Jin, A. Sanders, W. Park and W. Zhang, *J. Am. Chem. Soc.*, 2014, **136**, 1782–1785.
- (4) M. Mastalerz, *Angew. Chem. Int. Ed.*, 2010, **49**, 5042–5053.
- (5) T. R. Cook, Y. R. Zheng and P. J. Stang, *Chem. Rev.*, 2013, **113**, 734–777.
- (6) C. M. Erben, R. P. Goodman and A. J. Turberfield, *Angew. Chem. Int. Ed.*, 2006, **45**, 7414–7417.
- (7) T. G. W. Edwardson, K. M. M. Carneiro, C. K. McLaughlin, C. J. Serpell and H. F. Sleiman, *Nat. Chem.*, 2013, **5**, 868–875.
- (8) Y. T. Lai, D. Cascio and T. O. Yeates, *Science*, 2012, **336**, 1129–1129.
- (9) M. Kim, Y. Rho, K. S. Jin, B. Ahn, S. Jung, H. Kim and M. Ree, *Biomacromolecules*, 2011, **12**, 1629–1640.
- (10) G. Jutz, P. van Rijn, B. S. Miranda and A. Böker, *Chem. Rev.*, 2015, **115**, 1653–1701.
- (11) Y. Ueda, H. Ito, D. Fujita and M. Fujita, *J. Am. Chem. Soc.*, 2017, **139**, 6090–6093.
- (12) D. Fujita, Y. Ueda, S. Sato, N. Mizuno, T. Kumasaka and M. Fujita, *Nature*, 2016, **540**, 563–566.
- (13) D. H. Hubert, M. Jung and A. L. German, *Adv. Mater.*, 2000, **12**, 1291–1294.
- (14) M. S. Yavuz, Y. Cheng, J. Chen, C. M. Cobley, Q. Zhang, M. Rycenga, J. Xie, C. Kim, K. H. Song, A. G. Schwartz, L. V. Wang and Y. Xia, *Nat. Mater.*, 2009, **8**, 935–939.
- (15) T. R. Cook and P. J. Stang, *Chem. Rev.*, 2015, **115**, 7001–7045.
- (16) D. Zhang, A. Martinez and J. P. Dutasta, *Chem. Rev.*, 2017, **117**, 4900–4942.
- (17) S. Durot, J. Taesch and V. Heitz, *Chem. Rev.*, 2014, **114**, 8542–8578.
- (18) J. M. Lehn, *Pure Appl. Chem.*, 1978, **50**, 871–892.
- (19) Tezuka, Y. Topological Polymer Chemistry for Designing Multicyclic Macromolecular Architectures. *Polymer J.*, **2012**, *44*, 1159–1169.
- (20) Y. Tezuka, A. Tsuchitani, Y. Yoshioka and H. Oike, *Macromolecules*, 2003, **36**, 65–70.
- (21) M. Igari, H. Heguri, T. Yamamoto and Y. Tezuka, *Macromolecules*, 2013, **46**, 7303–7315.

- (22) Y. Tezuka and K. Fujiyama, *J. Am. Chem. Soc.*, 2005, **127**, 6266–6270.
- (23) K. Kyoda, T. Yamamoto and Y. Tezuka, *J. Am. Chem. Soc.*, 2019, **141**, 7526–7536.
- (24) J. Jeong, K. Kim, R. Lee, S. Lee, H. Kim, H. Jung, M. A. Kadir, Y. Jang, H. B. Jeon, K. Matyjaszewski, T. Chang and H.-j. Paik, *Macromolecules*, 2014, **47**, 3791–3796.
- (25) J. Zhao, Y. Zhou, Y. Li, X. Pan, W. Zhang, N. Zhou, K. Zhang, Z. Zhang and X. Zhu, *Polym. Chem.*, 2015, **6**, 2879–2891.
- (26) A. K. Mohanty, J. Ye, J. Ahn, T. Yun, T. Lee, K.-s. Kim, H. B. Jeon, T. Chang and H.-j. Paik, *Macromolecules*, 2018, **51**, 5313–5322.
- (27) T. Lee, J. Oh, J. Jeong, H. Jung, J. Huh, T. Chang and H.-j. Paik, *Macromolecules*, 2016, **49**, 3672–3680.
- (28) Y. Mato, K. Honda, K. Tajima, T. Yamamoto, T. Isono and T. Satoh, *Chem. Sci.*, 2019, **10**, 440–446.
- (29) M. Gauthier-Jaques and P. Theato, *ACS Macro Lett.*, 2020, **9**, 700–705.
- (30) T. Noda, Y. Doi, Y. Ohta, S.-i. Takata, A. Takano and Y. Matsushita, *J. Polym. Sci.*, 2020, **58**, 2098–2107.
- (31) Y. Satoh, H. Matsuno, T. Yamamoto, K. Tajima, T. Isono and T. Satoh, *Macromolecules*, 2017, **50**, 97–106.
- (32) L. Xiang, W. Ryu, H. Kim and M. Ree, *Polymers*, 2018, **10**, 577.
- (33) W. Ryu, L. Xiang, T. Jeon and M. Ree, *Polymer*, 2020, **207**, 122899.
- (34) L. Xiang, W. Ryu, J. Kim and M. Ree, *Polym. Chem.*, 2020, **11**, 4630–4638.
- (35) Y. Y. Kim, B. J. Ree, M. Kido, Y.-G. Ko, R. Ishige, T. Hirai, D. Wi, J. Kim, W. J. Kim, A. Takahara, M. Ree, *Adv. Electron. Mater.*, 2015, **1**, 1500197.
- (36) H. Brittiger, R. H. Marchessault and W. D. Niegisch, *Acta Crystallogr. Sect. B*, 1970, **26**, 1923–1927.
- (37) Y. Y. Kim, S. Jung, C. Kim, B. J. Ree, D. Kawato, N. Nishikawa, D. Suemasa, T. Isono, T. Kakuchi, T. Satoh, M. Ree, *Macromolecules*, 2014, **47**, 7510–7524.